SOLUTION OF THE COMPRESSIBLE NAVIER-STOKES EQUATIONS

FOR A DOUBLE THROAT NOZZLE

F. Bassi

Dip. di Energetica, P.zza L. da Vinci 32 Milano Italy 20133

F. Grasso

Ist. di Gasdinamica, P.le Tecchio 80, Napoli, Italy 80125

A. Jameson, L. Martinelli

Dept. of Mech. and Aero. Eng., Princeton, N.J. 08544

M. Savini

Ist. Ric. Prop. e Energetica, CNR, V.le Baracca 69, Peschiera Borromeo
(Milano), Italy 20068

SUMMARY

An explicit multistage finite volume method for the solution of the compressible Navier Stokes equations has been applied to resolve the transonic flow through a double throat nozzle. The accuracy and robustness of the method are shown by the accurate predictions of: extent of recirculation regions; effects of the Reynolds number on the shock structure; the viscous-inviscid interaction. The dependency of the solution upon grid refinement and wall boundary condition is also studied.

INTRODUCTION

The numerical solution of the compressible Navier Stokes equations (CNS) is a severe test for most numerical algorithms as far as accuracy and robustness of the methods are concerned, on account of the complexities of the flows to be simulated.

In the last decade several implicit or semimplicit algorithms have been developed [1]-[5]. The progress in high speed computers and in the development of efficient numerical methods for the solutions of the Euler equations [6]-[7] have stimulated the application of explicit algorithms to CNS [8]-[10].

In the present work the viscous transonic flow through a double throat nozzle is analized by using an explicit multistage finite volume method. The objective of the work is to assess the accuracy and the robustness of

the method in the presence of recirculation regions and strong viscous-inviscid interactions.

The numerical algorithm is an extension of that developed for the solution of the Euler equations by Jameson [11]. A cell centered formulation (i.e. the flow variables are defined at cell centers) is employed so as to use a fully conservative form of the Navier Stokes equations. However, as already pointed out in Ref. [10], such an approach requires some interpolation to satisfy Dirichlet boundary conditions for temperature, as requested in the test cases.

The computations have been performed on H-type meshes, best suited for the present applications. Two different grid refinements and two different nodal point distributions have been used to study the influence of the discretization on the solution.

The test cases require to compute the flow for three different values of the Reynolds number. The computed results show that the present method is able to predict the main features of the flow with good agreement with the results obtained by others.

In the next sections the governing equations are presented, then the numerical algorithm is discussed together with the treatment of the boundary conditions and the grid generation technique. Finally the results and some concluding remarks are given.

GOVERNING EQUATIONS

In the present approach a fully conservative formulation of the compressible Navier Stokes equations is employed. The dimensionless form of the equations is obtained by choosing the following reference quantities:

$$x_r, y_r = L \qquad t_r = \frac{L}{c_0} \qquad \rho_r = \rho_0 \qquad P_r = \gamma P_0$$

$$u_r = c_0 \qquad E_r = c_0^2 \qquad \mu_r = \frac{\rho_0 c_0 L}{Re} \qquad \lambda_r = \frac{c_0 \mu_r}{Pr}$$

where L, c, Re and Pr are respectively the half throat nozzle height, the speed of sound, the Reynolds and the Prandtl numbers.

In a cartesian coordinate system the equations are:

$$\frac{\partial}{\partial t} \int_V w \, dV + \oint_{\partial V} (f n_x + g n_y) \, dS = \oint_{\partial V} (P n_x + Q n_y) \, dS$$

where w, f, g, P and Q are respectively the vector unknown, the non dissipative flux components in x and y direction and the diffusive flux components in x and y, and they are defined as follows:

$$w = [\rho, \rho u, \rho v, \rho E]^T$$

$$f = [\rho u, \rho u^2 + p, \rho uv, \rho uE + up]^T$$

$$g = [\rho v, \rho uv, \rho v^2 + p, \rho vE + vp]^T$$

$$P = [0, \sigma_{xx}, \sigma_{xy}, u\sigma_{xx} + v\sigma_{xy} - q_x]^T$$

$$Q = [0, \sigma_{xy}, \sigma_{yy}, u\sigma_{xy} + v\sigma_{yy} - q_y]^T$$

where u and v are the velocity components in x and y; e, p and E are respectively the density, pressure and total energy.

Equation of state

$$p = (\gamma - 1) [E - 1/2(u^2 + v^2)]$$

Constitutive equations

$$\underline{\underline{\sigma}} = \frac{1}{Re} [(\nabla \underline{u} + \nabla \underline{u}^T) - 2/3 \nabla \cdot \underline{u} \; \underline{\underline{U}}]$$

$$\underline{q} = - \frac{\gamma}{RePr} \nabla e$$

where e, γ and $\underline{\underline{U}}$ are respectively the specific internal energy, the ratio of the specific heat coefficients and the unit tensor.

NUMERICAL SOLUTION

The computational domain is partitioned into arbitrary quadrilateral cells. The discretized form of the governing equations is obtained by applying Eqn. (1) to each cell and assuming that the flow variables are uniform within each computational volume. The spatial and temporal terms are decoupled by using the method of lines [11]-[12], and the system of governing equations is reduced to a system of ordinary differential equations (ODE).

The volume integrals are approximated by means of the mean value theorem, and the mid-point rule is employed for the surface integrals. The following ODE is obtained:

$$\frac{d}{dt} (Vw)_{ij} = - \underset{\beta=1,4}{\Sigma} \underbrace{[(\hat{f}n_x + \hat{g}n_y)\Delta S]_\beta}_{I} + \underset{\beta=1,4}{\Sigma} \underbrace{[(\hat{P}n_x + \hat{Q}n_y) \Delta S]_\beta}_{II} \qquad (2)$$

where n_x and n_y are respectively the components of the positive unit normal in x and y.

The numerical flux $(\hat{f},\hat{g})$ at cell face β is evaluated as the average of the corresponding values at the two adjacent cells. This definition guarantees that $(\hat{f},\hat{g})$ be consistent with (f,g) in the following sense:

$$\hat{f}(w,w) = f(w)$$

$$\hat{g}(w,w) = g(w)$$

moreover it enhances the computational efficiency and it yields second order accuracy on a smooth grid. Observe that term I coincides with the Euler-type flux contribution (R_E).

The discretized counterpart of the diffusion fluxes ($\hat{P}, \hat{Q}$) are evaluated by applying Gauss theorem to a computational volume centered around a grid node and whose vertices are the centers of the four adjacent cells, so as to calculate the velocity and temperature gradients [10], [12].

Adaptive dissipative terms, proportional to the second and fourth differences of the variables, are added to the discretized governing equations to prevent even/odd decoupling and to inhibit expansion shocks [11], when solving the Euler equations. The Navier Stokes equations contain physical dissipative terms. However some adaptive dissipation is still added to guarantee the proper behaviour of the scheme in regions where the convection and diffusion contributions are not of the same order. Hence Eqn. (2) is augmented by adding adaptive dissipation terms similar to the ones employed in Euler calculations [10]-[11], yielding:

$$\frac{d}{dt}(Vw)_{ij} = -R_E(w) - D(w) - AD(w) \tag{3}$$

where D represents term II of Eqn. (2), and AD is the adaptive dissipation.

The time integration of Eqn. (3) is obtained by employing an explicit 3-stage Runge-Kutta scheme as that used in ref. [10]. To enhance the computational efficiency both the physical and artificial dissipative terms are evaluated once per time step. The solution is then advanced in time as follows:

$$w^{(0)} = w^n$$

$$w^{(1)} = w^{(0)} - \alpha_1 \Delta t/V[R_E^{(0)} + D^{(0)} + AD^{(0)}]$$

$$w^{(2)} = w^{(0)} - \alpha_2 \Delta t/V[R_E^{(1)} + D^{(0)} + AD^{(0)}]$$

$$w^{n+1} = w^{(0)} - \Delta t/V[R_E^{(2)} + D^{(0)} + AD^{(0)}]$$

where $\alpha_1 = \alpha_2 = .6$.

The efficiency of the method is further increased by use of local time stepping and implicit smoothing.

Mesh Description

The mesh used in the computations is a body fitted H-mesh obtained by solving the Laplace equation for the stream function (ψ) on an equally spaced grid that covers the physical domain. The coordinates of the nodes are obtained by finding lines of constant ϕ (the velocity potential) and constant ψ, yielding a system of orthogonal grid coordinate lines.

To improve viscous layer resolution the grid is refined near the wall. The refinement is accomplished by use of the following nodal point distribution (along ψ) [13]:

$$f(\psi) = m\psi + (1-m)[1 - \frac{\tanh D(1-\psi)}{\tanh\psi}]$$

where D measures the rate of deviation from a uniform linear distribution with slope m.

Boundary Conditions

At the wall no slip boundary conditions are imposed on the velocity components, i.e.

$$\underline{u} \cdot \underline{n} = 0$$

$$\underline{u} \cdot \underline{t} = 0$$

The temperature is set equal to the stagnation value as requested in the test cases.

The pressure is needed at the wall when evaluating the momentum balance equation for the cells adjacent to the solid boundary. For this purpose two different boundary conditions are investigated:

$$\nabla p \cdot \underline{n} = 0 \tag{4}$$

$$(-\nabla p + \nabla \cdot \underline{\underline{\sigma}}) \cdot \underline{n} = 0 \tag{5}$$

Computations performed using either Eqn. (4) or (5) have shown negligible differences in the results.

Due to symmetry of the flow, symmetry boundary conditions are imposed along the centerline axis.

At the upstream boundary the viscous effects are neglected and the following boundary conditions are imposed (being $M_0 < 1$):

$$H = H_0 \tag{6}$$

$$s = s_0 \tag{7}$$

$$\frac{2}{\gamma-1} c + q_n = \frac{2}{\gamma-1} c_e + q_{n_e} \tag{8}$$

$$q_n n_y - q_t n_x = 0 \tag{9}$$

where n_x, n_y are the components of the normal to the surface, positive if pointing outward; q_n, q_t, H and s are respectively the normal and tangential velocity components, the total enthalpy and the entropy.

Eqn. (8) corresponds to a boundary condition for the outgoing Riemann invariant. Eqn. (9) implies that the flow be parallel to the centerline axis.

At the downstream boundary, numerical boundary conditions are obtained by extrapolation from the interior in the direction normal to the outflow

surface, i.e.

$$\frac{\hat{\partial}^2}{\partial n^2} \left(\frac{2c}{\gamma - 1} + q_n\right) = 0 \tag{10}$$

$$\frac{\hat{\partial}^2 s}{\partial n^2} = 0 \tag{11}$$

$$\frac{\hat{\partial}^2 q_t}{\partial n^2} = 0 \tag{12}$$

$$\frac{\hat{\partial}^2}{\partial n^2} \left(\frac{-2c}{\gamma - 1} + q_n\right) = 0 \tag{13}$$

where $\hat{\ }$ stands for numerical discretization.

Observe that Eqn. (13), valid only for locally supersonic flow, is used also in the subsonic case, as required in the specifications of the test cases.

RESULTS

The calculations for the three test cases at Re = 100; 400; 1600 have been performed on a 152x32 grid (Fig. 1) with the nodal point distribution of Fig. 2. The effects of mesh refinement and those due to the two different wall pressure boundary conditions (Eqn. (4)-(5)) have been studied at Re = 100.

All the computations have been performed on a GOULD 3267 (2 Mbytes CPU memory, 2 Mips). The computational times are given in table 1 and they correspond to a number of time steps $N \simeq 300/hr$, on a 152x32 grid without multigrid.

Re = 100 (CASE 1.A)

The flow variables have been initialized assuming uniform conditions corresponding to an inlet Mach number of .4. To drive the flow to a fully expanded situation all but Eqn. (13) are imposed at the outflow. Indeed the fourth boundary conditions has been set by imposing a pressure corresponding to an isentropic Mach number equal to 1.3 until a supersonic region develops. After that the outflow boundary conditions (Eqns. (10)-(13) are imposed.

Figs. 3-11 show the strong influence of the viscous effects and an extended recirculation region between the two throats as indicated by the wall skin friction distribution and the velocity profiles vs x.The flow separates at x_s =2.9788 and reattaches at x_R = 4.8343. Observe that for this case, strong recompression regions are absent .

Effects of Mesh Refinement (CASE 1.B-C)

Results obtained on a 152x32 grid with a high mesh refinement near the wall (see Figs. 30-35) indicate that, at least for such a low Reynolds number, it is not necessary to concentrate as many grid points near the wall. The level of convergence is worse than in the previous case as observed by comparing the mass flow rate along the channel for the two cases .

Comparison of the results obtained on the coarser mesh (102x22) show that the overall resolution of the flow field is adequate except through the compression region located downstream of the first throat (see Figs.36-41). Further differences are observed in the distribution of the heat flux coefficient vs x. However the differences seem due to the higher convergence reached on the 102x22 mesh.

Effects of the Wall Pressure Boundary Conditions (CASE 1.D)

Figs. 42-44 show the results obtained with the wall boundary conditions on pressure $\nabla p \cdot \underline{n} = 0$. The results indicate that the boundary layer approximation is adequate when using a highly refined mesh near the wall.

Re = 400 (CASE 2)

The flow variables have been initialized from the converged solution obtained at Re = 100. The isobar and isomach lines (Figs. 12-14), as well as the pressure and Mach distributions on the centerline (Figs. 15-20), show the formation of a rather strong shock. The interaction of the latter with the viscous zone is responsible for the delay in the flow reattachment as observed from Fig. 18 (x_s=3.0025; x_R=6.2829). Due to the viscous layer thickness reduction, the mass flow rate increases with respect to the one at Re = 100, as it appears from Fig. 19, which also shows the good convergence of the computation.

Re = 1600 (CASE 3)

The flow field has been initialized starting from the converged solution at Re = 400. At the Reynolds number 1600, apart from the viscous zone, the flow is supersonic from the first throat to the outlet section. The shock structure becomes oblique and the extent of the recirculation zone between the two throats is reduced: x_s=3.4006; x_R=4.7669 (see Figs. 21-29). A second recirculation bubble appears just downstream of the second throat due to the interaction between the impinging oblique shock and the viscous layer (x_s=8.0326; x_R=8.2560).

CONCLUSIONS

An explicit 3-stage finite volume method for the solution of the compressible Navier Stokes equations has been applied to resolve the transonic flow through a double throat nozzle at different Reynolds numbers. The efficiency of the method is increased by using local time stepping, implicit smoothing and a cell centered formulation. The main features of the flow (extent of recirculation regions, location of the points of separation and reattachment, effects of the Reynolds number on the shock structure, viscous-inviscid interaction) have been accurately predicted.

The effect of different mesh refinements and different nodal point distributions have been studied at Re = 100. At this Reynolds number, the computed results show no need for using very refined meshes. However an adaptive local mesh refinement should be used to improve the accuracy [14], [15] at higher Reynolds numbers, where the flow structure is such that large gradients of the variables arise in small regions.

To enhance the computational efficiency of the method a multigrid technique should also be used [10], [11].

REFERENCES

[1] Steger J.L., "Implicit Finite Difference Simulation of Flow About Arbitrary Geometries with Applications to Airfoils", AIAA paper no. 77-665, 1977.

[2] Beam, R. and Warming, R., "An implicit Factored Scheme for the Compressible Navier-Stokes Equations", AIAA J. Vol. 16, 1978.

[3] Briley, W.R. and Mc Donald, H., "Solution of the Multi-Dimensional Compressible Navier-Stokes Equations by a Generalized Implicit Method", J. of Comp. Physics, Vol. 24, 1977.

[4] Barth, J., Pulliam, T. and Bunning, P., "Navier Stokes Computations for Exotic Airfoils", AIAA paper no. 85-0109, 1985.

[5] Ong, C. and Knight, D., "A Comparative Study of the Hybrid MacCormack and Implicit Beam-Warming Algorithms for a Two-Dimensional Supersonic Compression Corner," AIAA paper no. 86-0204, 1986.

[6] Jameson, A., Schmidt, W. and Turkel, E., "Numerical Solutions of the Euler Equations by Finite Volume Methods Using Runge-Kutta Time-Stepping Schemes," AIAA paper no. 81-1259, 1981.

[7] Jameson, A., Baker, J. and Weatherhill, N., "Calculation of the Inviscid Transonic Flow over a Complete Aircraft," AIAA paper no. 86-0103, 1986.

[8] Agarwaal, R. and Deese, L., "Computations of Transonic Viscous Airfoil, Inlet and Wing Flowfields," AIAA paper no. 84-1551, 1984.

[9] Swanson, R.C. and Turkel, E., "A Multistage Time-Stepping Scheme for the Navier Stokes Equations," AIAA paper no. 85-0035, 1985.

[10] Martinelli, L., Jameson, A. and Grasso, F., "A Multigrid Method for the Navier Stokes-Equations," AIAA paper no. 86-0208, 1986.
[11] Jameson, A., "Transonic Flow Calculations," MAE Report no.1651, Princeton University, 1983.
[12] Peyret, R. and Taylor T.D., "Computational Methods for Fluid Flow," Springer Verlag 1982.
[13] Eiseman, P.R., "Viscous Transonic Cascade Analysis," J. Comp. Physics Vol. 26, 1978.
[14] Berger, M. and Jameson, A., 9th ICNMFD, Saclay, France, 1985.
[15] Dannenhoffer, J.F. and Baron, J.R., "Grid Adaptation for the 2-D Euler Equations," AIAA paper no. 85-0484, 1985.

ACKNOWLEDGEMENT
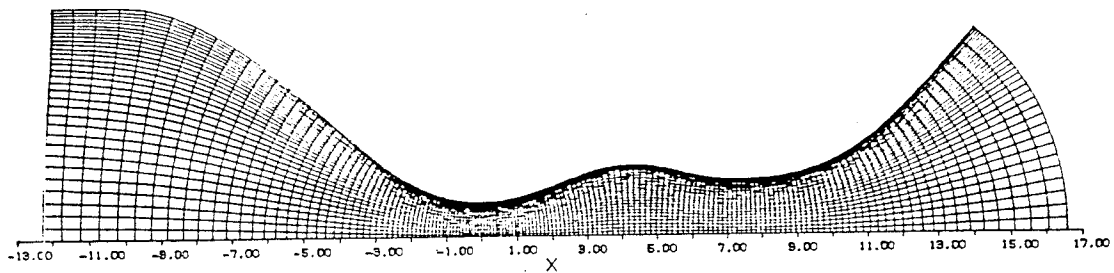
Fig. 1 - Computational Mesh (152x32)
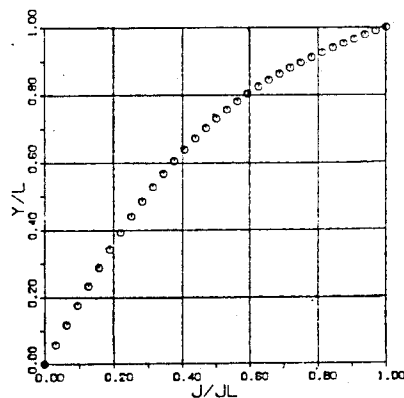
Fig. 2 - Mesh Point Distribution

Table 1 - CPU Time and Residual Values

| Re	Grid	CPU Gould 3267	$\log \text{RMS}(\frac{d\rho}{dt})$
100	152x32	1260	-3.9281
400	152x32	1000	-4.5302
1600	152x32	600	-4.5406
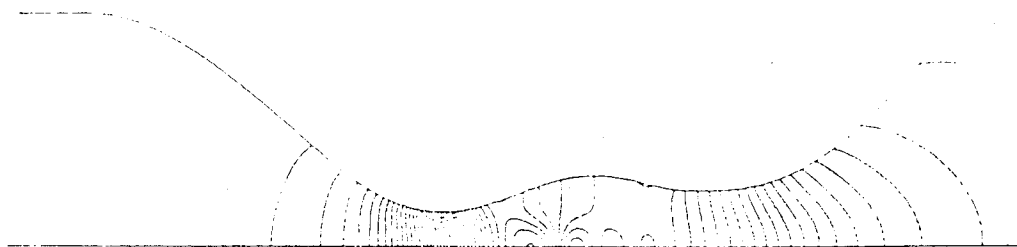
Fig. 3 - Pressure Contours (DP = .02)
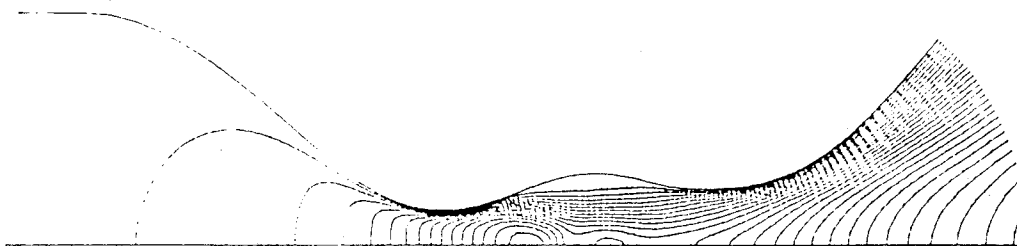
Fig. 4 - Mach Contours (DM = .1)
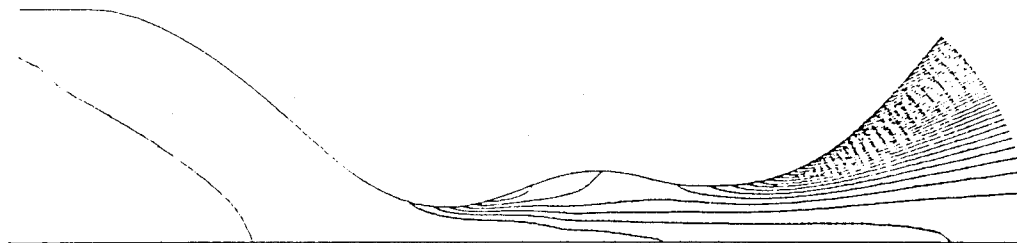
Fig. 5 - Entropy Contours (DS = .1)

Table 2 - RE = 100

: x :	-10	:	-4	:	0	:	4	:	7	:	13	:
p/p_c	.99661		.98346		.54908		.35386		.33556		.023897	
c_f	.0011264		.0071064		.0095134		-.0025015		.041744		.022022	
c_h	.47032E-5		.69091E-4		.007057		.0011061		.0035174		.0037657	
p/p_0	.99435		.97016		.59374		.40499		.34521		.070498	
M	.091126		.20912		.90042		1.14721		1.18759		2.16658	
S	.99995		1.00008		1.00041		1.05225		1.11369		1.18381	

WALL VALUES (rows p/p_c, c_f, c_h)

SYMMETRY AXIS VALUES (rows p/p_0, M, S)
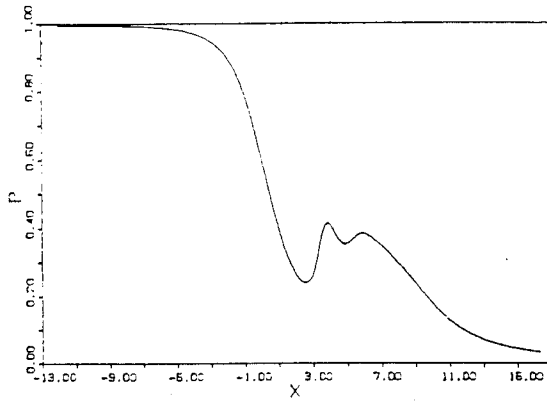
Fig. 6 - Centerline Pressure
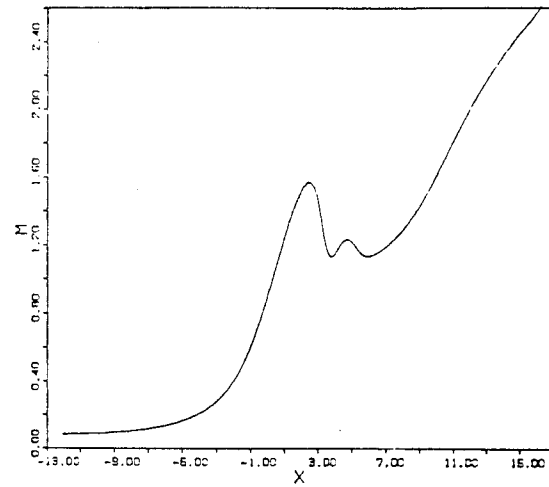
Fig. 7 - Centerline Mach Number
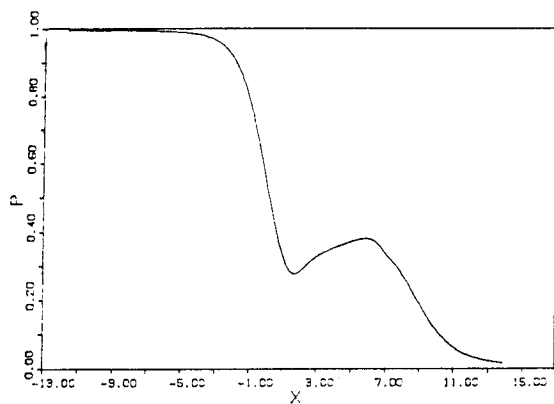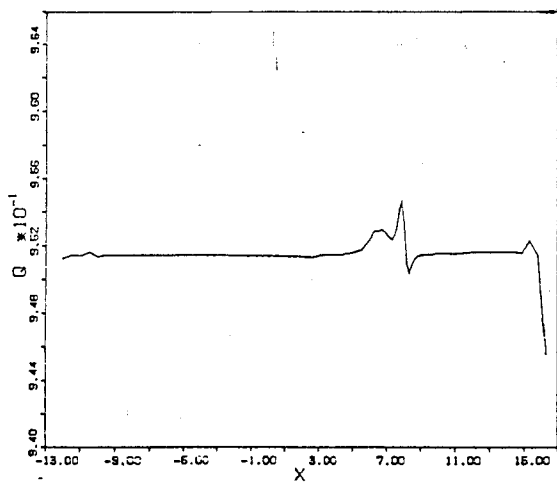
Fig. 8 - Wall Pressure
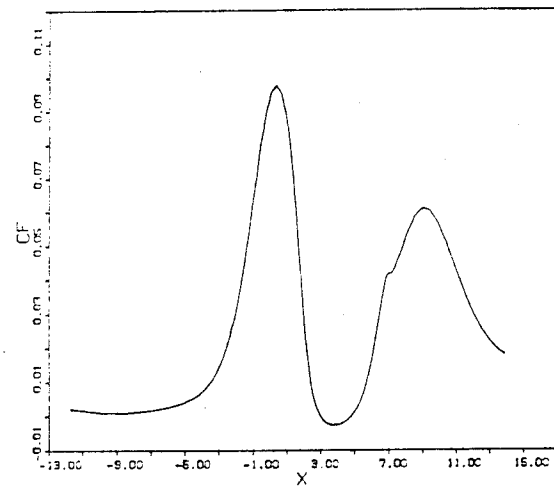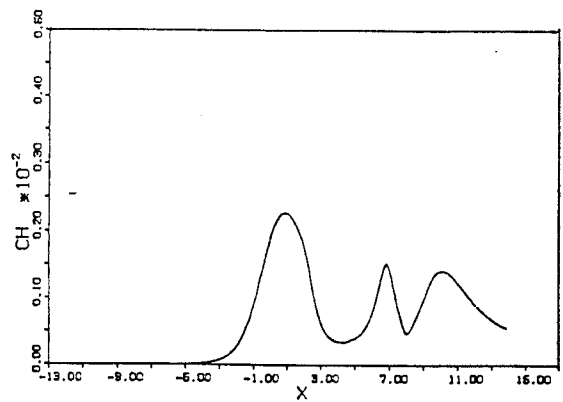
Fig. 9 - Wall Skin Friction
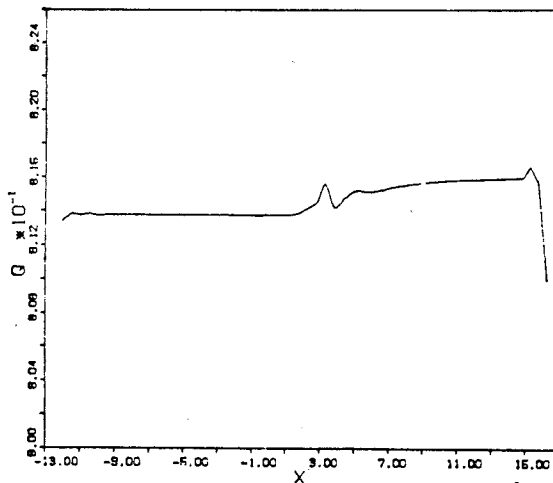
Fig. 10 - Mass Flow Rate
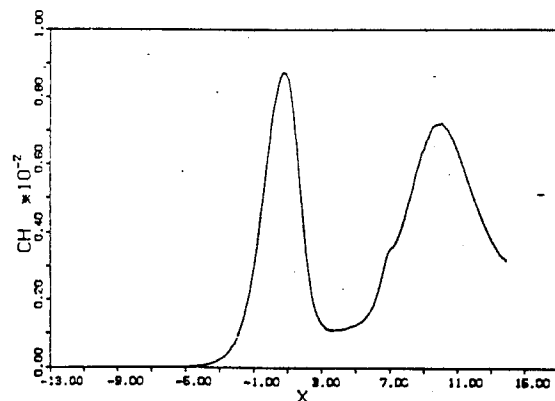
Fig. 11 - Wall Heat Flux

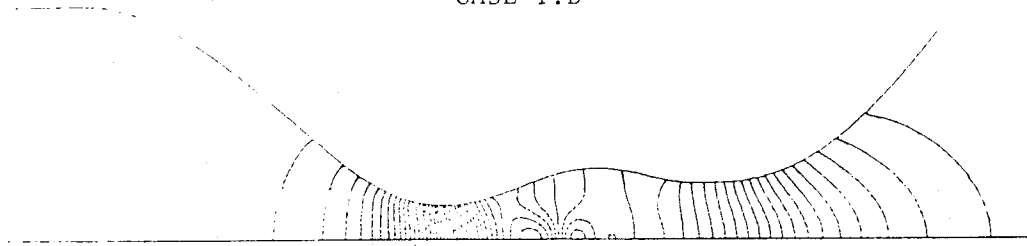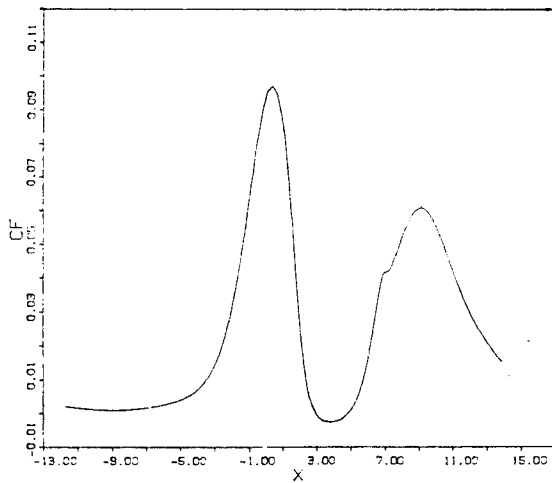Fig. 12 - Pressure Contours (DP = .02)
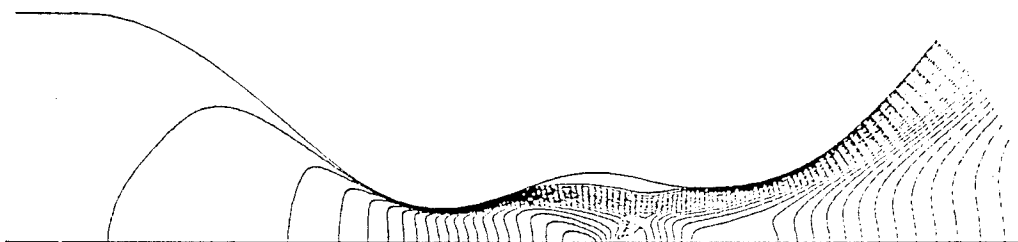
Fig. 13 - Mach Contours (DM = .1)
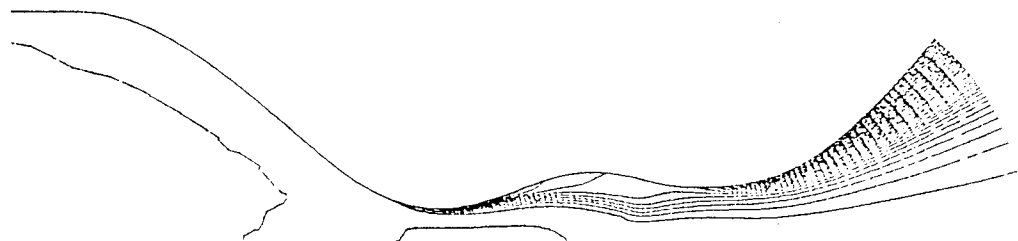
Fig. 14 - Entropy Contours (DS = .1)

Table 3 - RE = 400

	x	-10	-4	0	4	7	13
WALL VALUES	p/p_0	.99638	.98117	.512455	.25509	.28135	.18906
	c_f	.4717E-3	.0039085	.049432	-.00219	.015262	.0095716
	c_h	.23642E-5	.45368E-4	.0036684	.48878E-3	.001548	.0015795
SYMMETRY AXIS VALUES	$p/\bar{p_0}$	.99357	.96778	.57570	.11183	.22272	.06108
	M	.096811	.21703	.92619	2.08007	1.5906	2.42434
	S	.99996	1.00002	.9995	1.00341	1.027	1.0324
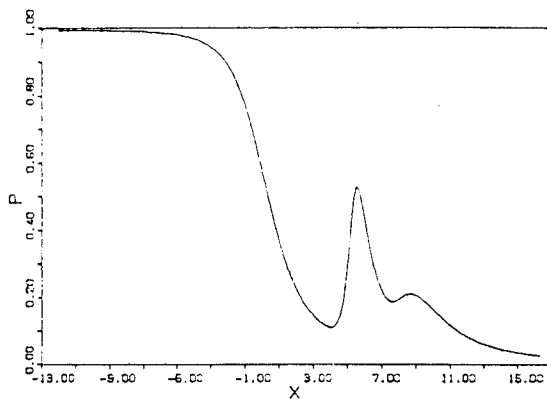
Fig. 15 - Centerline Pressure
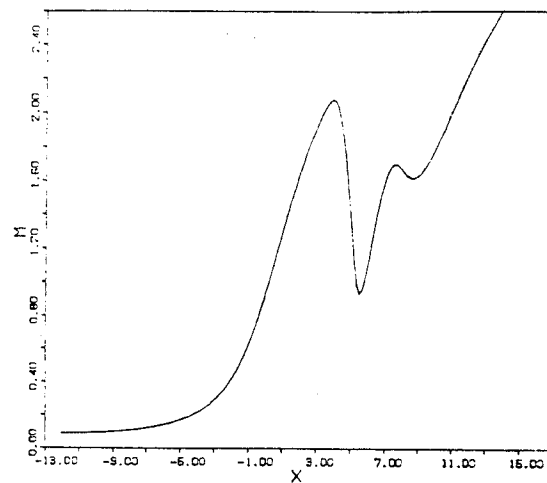
Fig. 16 - Centerline Mach Number
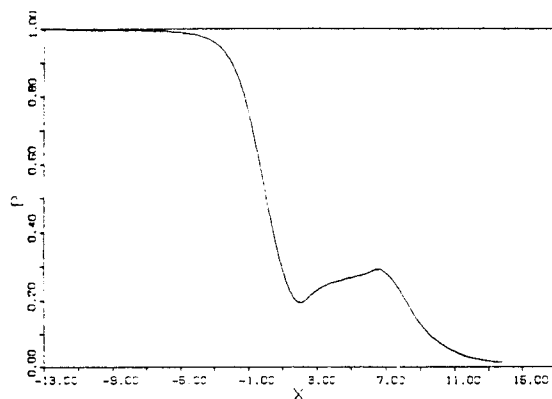
Fig. 17 - Wall Pressure
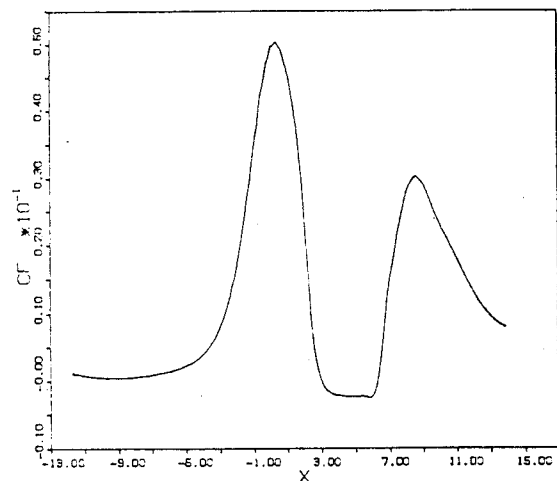
Fig. 18 - Wall Skin Friction
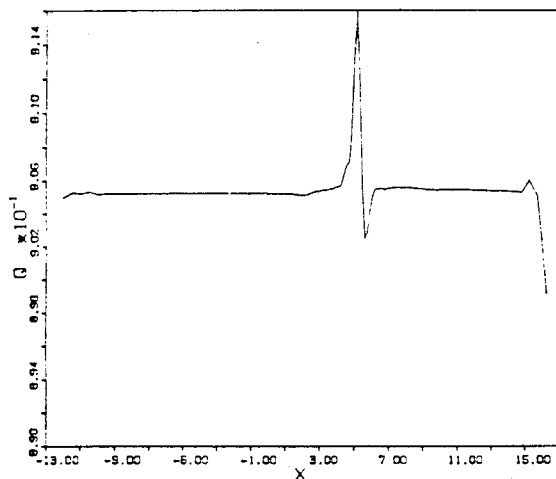
Fig. 19 - Mass Flow Rate
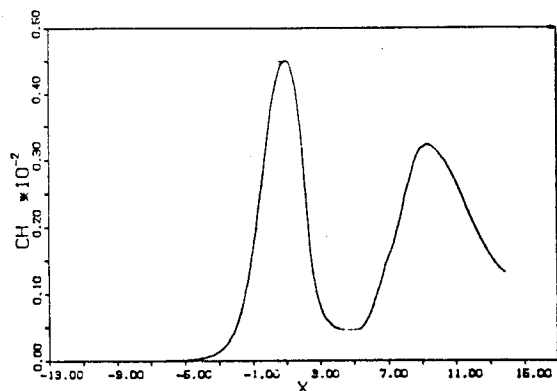
Fig. 20 - Wall Heat Flux
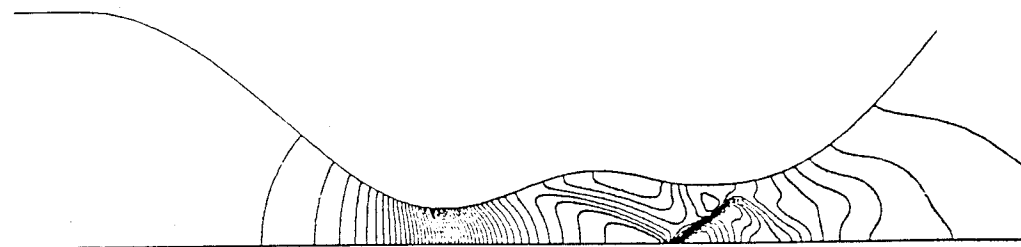
Fig. 21 - Pressure Contours (DP = .02)
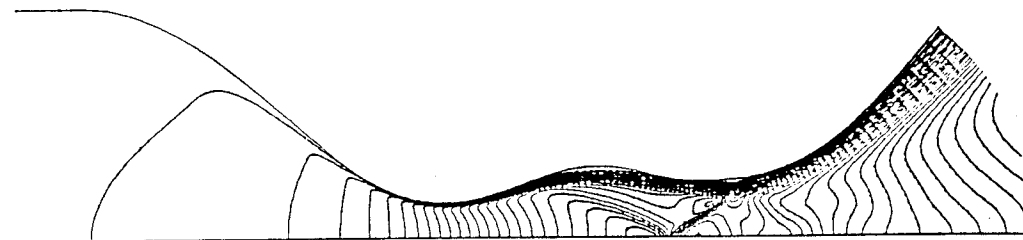
Fig. 22 - Mach Contours (DM = .1)
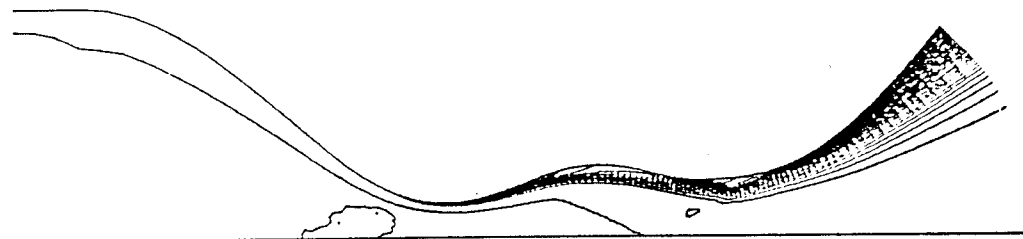
Fig. 23 - Entropy Contours (DS = .1)

Table 4 - RE = 1600

	x	-10	-4	0	4	7	13
WALL VALUES	p/p_0	.99625	.98005	.49071	.19565	.12673	.014435
	c_f	.21724E-3	.0021475	.02526	-.67258E-3	.013253	.004195
	c_h	.24654E-6	.25331E-4	.0019085	.35770E-3	.0014171	.68152E-3
SYMMETRY AXIS VALUES	p/p_0	.99317	.96640	.56657	.094517	.33586	.050162
	M	.099733	.22163	.93948	2.19385	1.30375	2.55742
	s	.99996	1.	.99976	.99964	1.0265	1.0254
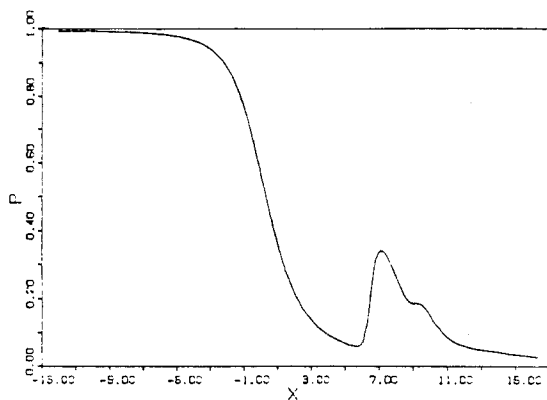
Fig. 24 - Centerline Pressure
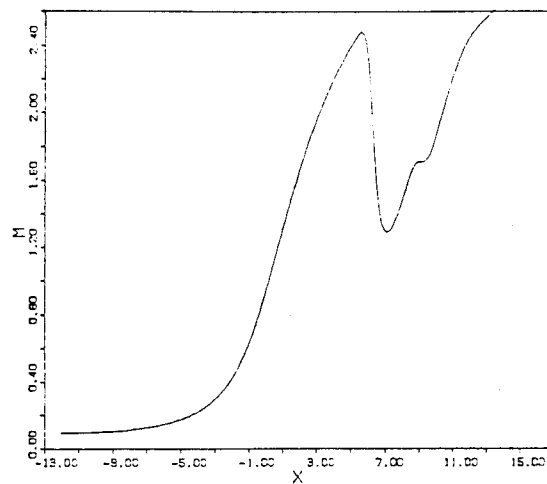
Fig. 25 - Centerline Mach Number
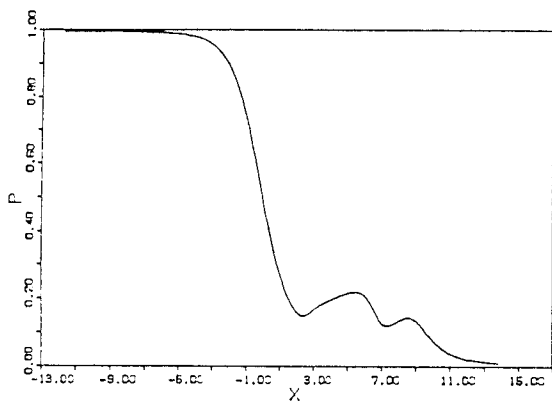
Fig. 26 - Wall Pressure
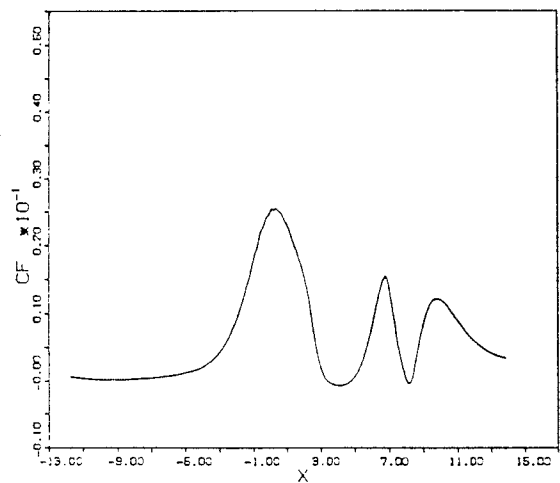
Fig. 27 - Wall Skin Friction

Fig. 28 - Mass Flow Rate

Fig. 29 - Wall Heat Flux
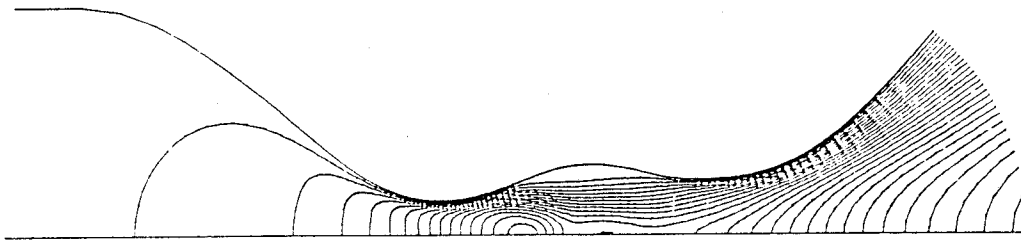
Fig. 30 - Pressure Contours (DP = .02)
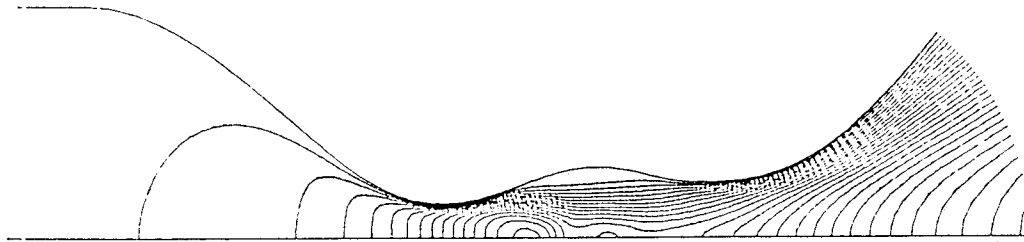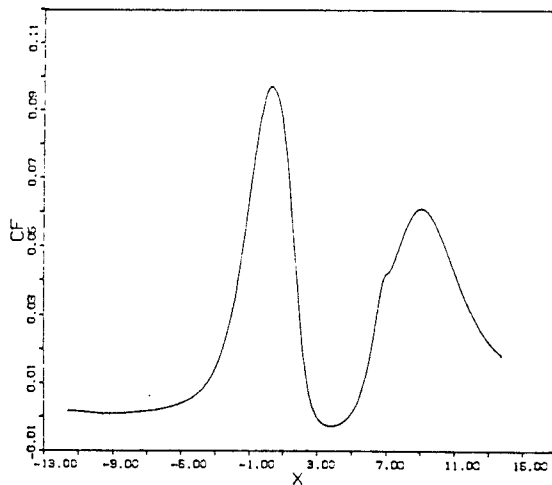
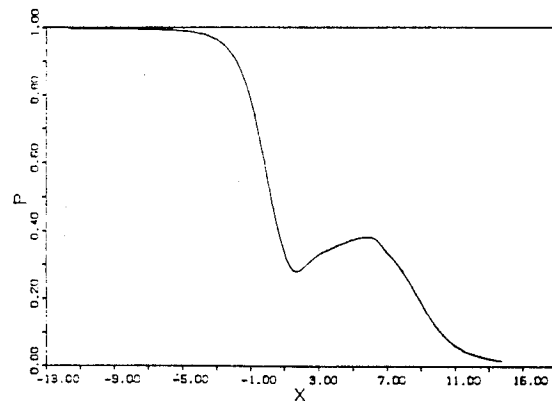Fig. 31 - Mach Contours (DM = .1)

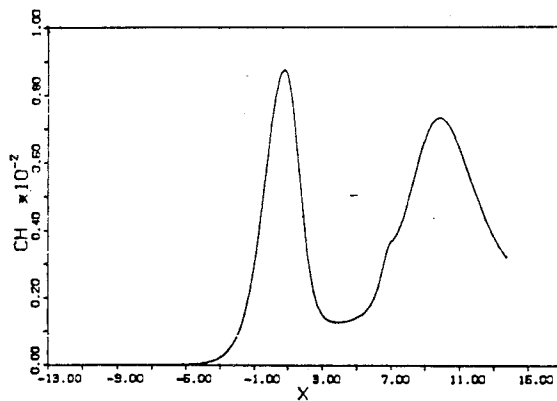Fig. 32 - Wall Skin Friction
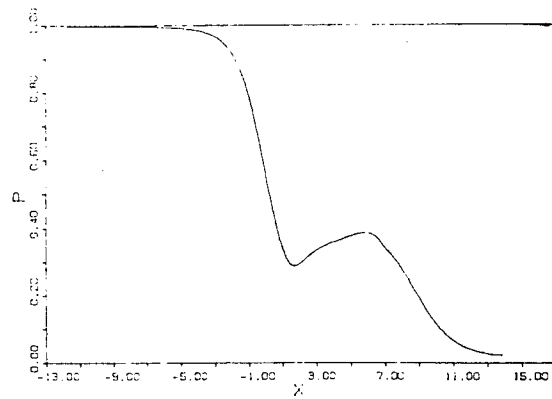
Fig. 33 - Wall Pressure
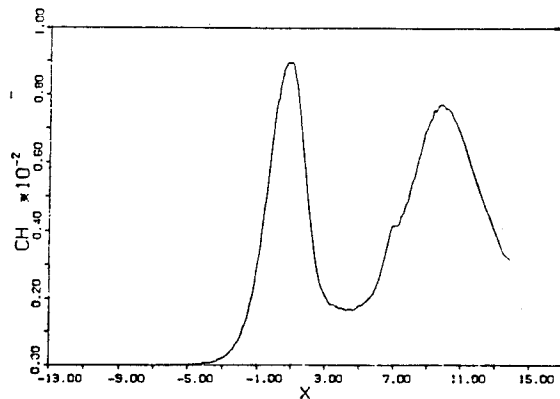
Fig. 34 - Wall Heat Flux
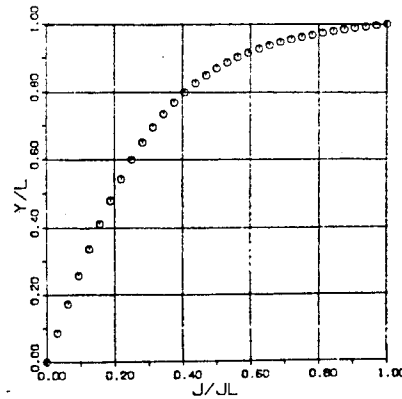
Fig. 35 - Mesh Point Distribution
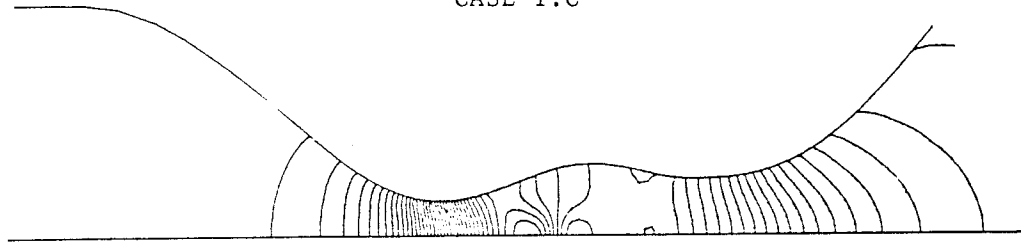
Fig. 36 - Pressure Contours (DP = .02)

Fig. 37 - Mach Contours (DM = .1)

Fig. 38 - Wall Skin Friction

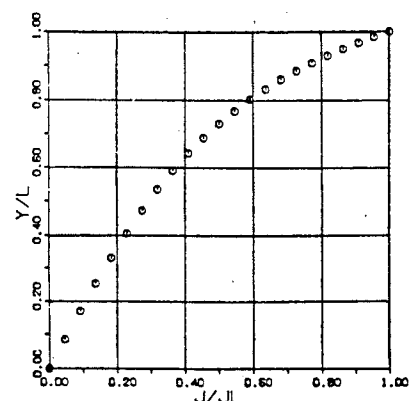Fig. 39 - Wall Pressure

Fig. 40 - Wall Heat Flux

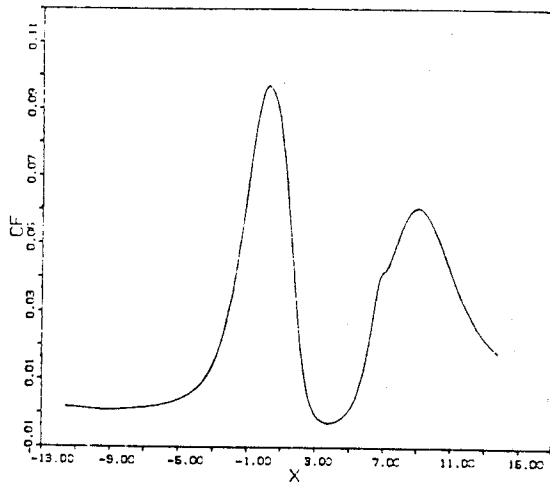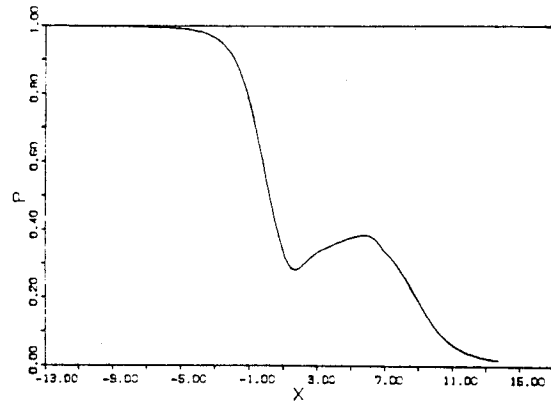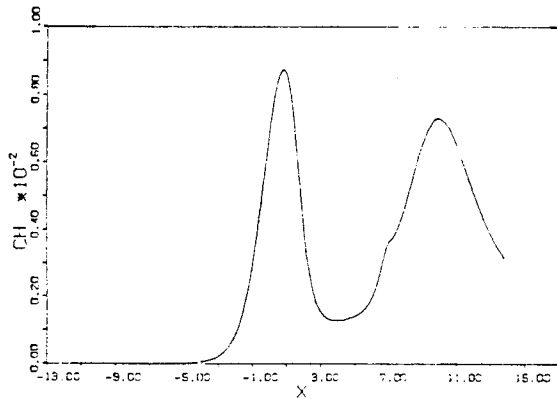Fig. 41 - Mesh Point Distribution

Fig. 42 - Wall Skin Friction

Fig. 43 - Wall Pressure

Fig. 44 - Wall Heat Flux